

An ALMA CO(2–1) Survey of Nearby Palomar-Green Quasars

JINYI SHANGGUAN,^{1,2} LUIS C. HO,^{2,3} FRANZ E. BAUER,^{4,5,6} RAN WANG,^{2,3} AND EZEQUIEL TREISTER⁴

¹*Max-Planck-Institut für Extraterrestrische Physik (MPE), Giessenbachstr., D-85748 Garching, Germany*

²*Kavli Institute for Astronomy and Astrophysics, Peking University, Beijing 100871, China*

³*Department of Astronomy, School of Physics, Peking University, Beijing 100871, China*

⁴*Instituto de Astrofísica and Centro de Astroingeniería, Facultad de Física, Pontificia Universidad Católica de Chile, Casilla 306, Santiago 22, Chile*

⁵*Millennium Institute of Astrophysics (MAS), Nuncio Monseñor Sótero Sanz 100, Providencia, Santiago, Chile*

⁶*Space Science Institute, 4750 Walnut Street, Suite 205, Boulder, Colorado 80301*

ABSTRACT

The properties of the molecular gas can shed light on the physical conditions of quasar host galaxies and the effect of feedback from accreting supermassive black holes. We present a new CO(2–1) survey of 23 $z < 0.1$ Palomar-Green quasars conducted with the Atacama Large Millimeter/submillimeter Array. CO emission was successfully detected in 91% (21/23) of the objects, from which we derive CO luminosities, molecular gas masses, and velocity line widths. Together with CO(1–0) measurements in the literature for 32 quasars (detection rate 53%), there are 15 quasars with both CO(1–0) and CO(2–1) measurements and in total 40 sources with CO measurements. We find that the line ratio $R_{21} \equiv L'_{\text{CO}(2-1)}/L'_{\text{CO}(1-0)}$ is subthermal, broadly consistent with nearby galaxies and other quasars previously studied. No clear correlation is found between R_{21} and the intensity of the interstellar radiation field or the luminosity of the active nucleus. As with the general galaxy population, quasar host galaxies exhibit a strong, tight, linear $L_{\text{IR}}-L'_{\text{CO}(1-0)}$ relation, with a normalization consistent with that of starburst systems. We investigate the molecular-to-total gas mass fraction with the aid of total gas masses inferred from dust masses previously derived from infrared observations. Although the scatter is considerable, the current data do not suggest that the CO-to-H₂ conversion factor of quasar host galaxies significantly differs from that of normal star-forming galaxies.

Keywords: galaxies: active — galaxies: evolution — galaxies: ISM — galaxies: Seyfert — (galaxies:) quasars: general — submillimeter: galaxies

1. INTRODUCTION

Molecular gas is a fundamental ingredient of the cold interstellar medium of galaxies, one that directly fuels star formation (Kennicutt 1998a; Bigiel et al. 2008) and accretion onto supermassive black holes (BHs; García-Burillo & Combes 2012; Combes et al. 2019; Storch-Bergmann & Schnorr-Müller 2019 and references therein). It is also a direct victim of the putative process of energy feedback from active galactic nuclei (AGNs; Fabian 2012). The properties of the molecular gas, therefore, are crucial to understand the coevolution of galaxies and their central BHs (Kormendy & Ho 2013; Heckman & Best 2014).

The cold interstellar medium of inactive, star-forming galaxies has been comprehensively investigated, both for the nearby (Saintonge et al. 2011a, 2017) and distant (Scoville et al. 2016; Tacconi et al. 2018) Universe. These studies have established empirical scaling relations among basic physical quantities, including gas mass, stellar mass, and star formation rate. Systematic studies of the cold gas in AGNs are still rare, particularly for objects luminous enough to be considered *bona fide* quasars.¹ Sensitivity limitations compelled early investigations to focus mainly on nearby AGNs or mostly quasars with strong far-infrared (IR) emission. While the molecular gas mass of nearby Seyfert galaxies is sim-

Corresponding author: Jinyi Shangguan
shangguan@mpe.mpg.de

¹ Following historical practice (Schmidt & Green 1983), we consider AGNs with $M_B < -23$ mag as quasars, regardless of their radio-loudness.

ilar to that of star-forming galaxies (matched in Hubble type and B -band luminosity), the star formation efficiency, as inferred from their extended far-IR emission, is higher among the Seyferts (Maiolino et al. 1997). Similarly, the $L_{\text{IR}}-L'_{\text{CO}(1-0)}$ relation of nearby quasars lies well above that of star-forming galaxies, which may indicate that the dust is heated by the quasar in addition to young stars (Evans et al. 2001, 2006). Irrespective of the detailed properties of the molecular medium, the existing data, scant though they may be, suggest that low-redshift, optically selected quasars reside in gas-rich host galaxies (Scoville et al. 2003).

Gas outflows, in molecular and other forms, have been observed in nearby AGNs (e.g., Cicone et al. 2014; Feruglio et al. 2015; Harrison et al. 2018; Herrera-Camus et al. 2019) and higher redshift ($z \gtrsim 1$) quasars (e.g., Maiolino et al. 2012; Bischetti et al. 2017; Brusa et al. 2018; Bischetti et al. 2019), plausibly interpreted as evidence of energy injection by so-called quasar-mode AGN feedback (Di Matteo et al. 2005; Hopkins et al. 2008; Fabian 2012). There is no consensus, however, as to whether AGN-driven outflows truly influence the cold gas content of AGN host galaxies (Ho et al. 2008; Cano-Díaz et al. 2012; Maiolino et al. 2012; Cresci et al. 2015; Carniani et al. 2016; Bischetti et al. 2017; Vayner et al. 2017; Baron et al. 2018; Brusa et al. 2018; Ellison et al. 2018; Perna et al. 2018; Shangguan et al. 2018; Shangguan & Ho 2019; Russell et al. 2019). High-redshift quasars are routinely detected with submillimeter tracers such as CO and [C II] $158 \mu\text{m}$, furnishing fundamental properties of their host galaxies (e.g., gas masses and dynamical masses) that would otherwise be inaccessible (Walter et al. 2004; Wang et al. 2013, 2016; Shao et al. 2017).

In this context, a comprehensive study of the local counterparts of high-redshift systems provides valuable insights into the coevolution of BHs and galaxies over cosmic time. Key questions still linger as to whether and how quasars affect the cold interstellar medium of their host galaxies. Are the basic properties of cold gas in quasar host galaxies different from those of inactive galaxies? Are there physical links between the properties of the active nuclei and the cold gas on large scales? Does star formation operate in the same manner as ordinary star-forming galaxies? Using CO(1–0) and CO(2–1) observations of a sample of 14 nearby quasars, Husemann et al. (2017) concluded that gas fraction and star formation efficiency depend on the host galaxy morphology. Gas fractions and gas depletion time scales in disk-dominated hosts resemble those of star-forming galaxies; bulge-dominated hosts, while generally more gas-poor, appear to exhibit higher star formation effi-

ciencies. AGN power correlates strongly with molecular gas mass, pointing to a plausible causal link between the two, but the overall gas content of the host galaxies does not appear to be depleted by quasar-mode feedback.

To enlarge the sample of nearby quasars with molecular gas measurements, we used the Atacama Large Millimeter/submillimeter Array (ALMA) to conduct a CO survey of a well-defined sample of 23 low-redshift ($z < 0.1$ and declination $< 30^\circ$) quasars selected from the Palomar-Green (PG; Schmidt & Green 1983) survey. It is important to recognize that the PG sample was originally ultraviolet-selected, and hence was not selected based on the dust or gas properties of the quasars. The high sensitivity of ALMA enabled us to detect CO(2–1) emission in 21 out of the 23 quasars, nearly doubling the number of CO detections of PG quasars known to date. Combined with previous results from the literature, we now have measurements of either CO(1–0) or CO(2–1) for a representative subset of 40 out of the parent sample of 70 PG quasars at $z < 0.3$, for which we provide self-consistent measurements of CO luminosity, molecular gas mass, and velocity line width. The focus of this paper is to describe our sample and present basic physical quantities for it. A companion paper (Shangguan et al. 2019b) investigates the possible connections between the properties of the AGN and the molecular gas.

We introduce the sample and observations in Section 2. The methods to derive the physical quantities are described in Section 3. Section 4 discusses the CO line ratio, the $L_{\text{IR}}-L'_{\text{CO}(1-0)}$ relation of quasar host galaxies, and the CO-to- H_2 conversion factor. We adopt the following cosmological parameters: $\Omega_m = 0.308$, $\Omega_\Lambda = 0.692$, and $H_0 = 67.8 \text{ km s}^{-1} \text{ Mpc}^{-1}$ (Planck Collaboration et al. 2016).

2. SAMPLE AND OBSERVATIONS

Our sample derives from the lower redshift subset of the ultraviolet/optically selected quasars from the PG survey. PG quasars have been extensively studied for decades, allowing us to take advantage of a wealth of available multiwavelength data. Shangguan et al. (2018) performed a comprehensive analysis of the IR spectral energy distributions of the 87 PG quasars with $z < 0.5$ (Boroson & Green 1992) to derive robust dust masses and total IR (8–1000 μm) luminosities of the host galaxies. They used the dust masses to infer global total (atomic plus molecular) gas masses. We directly use the 5100 Å AGN continuum luminosities, BH masses, and host galaxy stellar masses compiled by them. The stellar masses are derived from high-resolution optical/near-IR images with the nuclear emission decomposed (Zhang

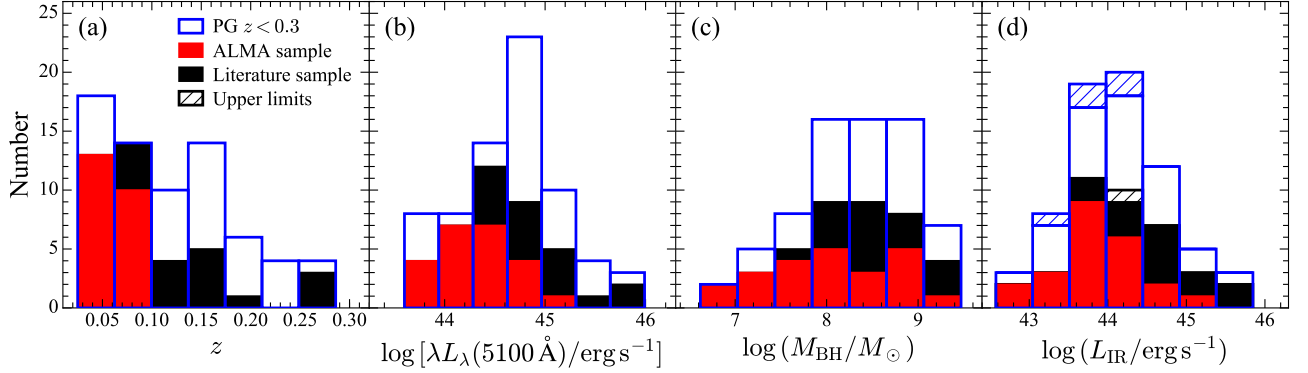


Figure 1. Comparison of the parent sample of 70 $z < 0.3$ PG quasars (blue) with the subsample of 40 PG quasars with CO measurements from our ALMA observations (red; 23 sources) and from the literature (black; 13 sources), in terms of (a) redshift, (b) 5100 Å AGN luminosity, (c) BH mass, and (d) total IR (8–1000 μm) luminosity. The hatched areas indicate the objects with L_{IR} upper limits.

et al. 2016).² For objects without stellar mass measurements, Shangguan et al. (2018) used bulge masses estimated from the $M_{\text{BH}}-M_{\text{bulge}}$ relation (Kormendy & Ho 2013). The axis ratio (q) of the host galaxy comes from two-dimensional GALFIT (Peng et al. 2002, 2010) decomposition of high-resolution optical and near-IR images acquired with the *Hubble Space Telescope* (Kim et al. 2017; Y. Zhao et al., in preparation).

We observed the $^{12}\text{CO}(2-1)$ 230.538 GHz line for all 23 PG quasars with $z < 0.1$ using the Band-6 receiver of the ALMA Compact Array (ACA) during Cycle 5 (PI: F. Bauer, 103.1 hours in total). The brightness of these nearby quasars allows to obtain significant detections using ACA with moderate resolving power ($\text{FWHM} \approx 6''$) in relatively short exposure times. Table 1 gives a summary of the observations. The flux and bandpass calibrators were observed in the beginning of each observation, and the phase calibrator was observed every $\sim 5 - 10$ minutes. The on-source integration times lasted between 120 and 280 min, typically 150 min. Integration times were estimated based on the CO(2–1) brightness expected from the AGN-decomposed IR luminosity of Shangguan et al. (2018), assuming that the $L_{\text{IR}}-L'_{\text{CO}(1-0)}$ relation is given by Equation (1) of Sargent et al. (2014) for starburst galaxies, adopting a CO line luminosity ratio $R_{21} \equiv L'_{\text{CO}(2-1)}/L'_{\text{CO}(1-0)} = 0.5$ (Xia et al. 2012). The data cube covers $\gtrsim 4000 \text{ km s}^{-1}$, spanning the full ~ 3.6 GHz spectral window of one sideband. The Hanning-smoothed spectral resolution is $\sim 5 \text{ km s}^{-1}$.

We reduced the data with the Common Astronomy Software Application³ (CASA; McMullin et al. 2007). The data were calibrated using the standard pipeline after minor flaggings of some problematic antennae and channels with sky absorption lines; this process did not affect the final results significantly. The continuum is subtracted with `uvcontsub`, fitting channels away from the line emission. Line images were constructed using the task `CLEAN` with robust weighting (`robust` = 0.5) and a stop threshold 2.5 times the root mean square (rms) of the off-source channels. The measured 1σ noise level per beam per channel (typically 1.5–5 mJy) is consistent within $\sim 30\%$ of the theoretical noise limit. To confirm that the ACA robust beam recovers all of the flux, we extracted fluxes using a $15''$ tapered beam, finding a 1:1 ratio within 3σ for all objects (Table 2).

Together with published $^{12}\text{CO}(1-0)$ data for 17 additional objects, there are CO measurements for 40 $z < 0.3$ PG quasars. Figure 1 compares the CO-measured subsample with the parent sample of 70 PG quasars with $z < 0.3$. Although the redshift distribution of the CO-measured objects is dominated by objects at $z \lesssim 0.1$, a two-sample Peto-Prentice test⁴ finds that the two redshift distributions are not statistically different; the probability of the null hypothesis that the distributions are drawn from the same parent sample is $P_{\text{null}} = 10.4\%$. The same holds for the distributions of 5100 Å AGN luminosity, BH mass, and IR luminosity, for which $P_{\text{null}} = 37.6\%$, 58.7% , and 71.3% , respectively.

³ <https://casa.nrao.edu>

² The stellar mass is not available from the decomposition of integrated spectral energy distribution, mainly due to the contamination of the overwhelming nuclear emission.

⁴ The Peto-Prentice test is adopted to work with samples including censored data (in our case, IR luminosity). It is equivalent to the Gehan test when there are no censored data.

We conclude that the CO-measured sample is representative of the parent sample of $z < 0.3$ PG quasars.

3. MEASUREMENTS

3.1. CO Luminosity

We use the channels above the 1σ level of the spectrum to generate the CO intensity (moment 0) map (Figure 2a). The integrated CO flux is measured from the intensity map by summing up the pixels within the 2σ contour of the source emission. We estimate the uncertainty from the standard deviation of 20 repeated off-source measurements using a circular aperture containing the same number of pixels as those within the 2σ contour of the source. The uncertainty of the absolute flux scale, $\sim 5\% - 10\%$ (Fomalont et al. 2014; Bonato et al. 2018), is not included in our final flux uncertainty. The integrated CO spectrum, used to measure the line width (Section 3.2), is extracted from the line-emitting region above 2σ of the intensity map. CO(2–1) was previously detected in PG 0050+124 using the JCMT (114 ± 23 Jy km s $^{-1}$; Papadopoulos et al. 2008) and in PG 1126–041 using IRAM 30 m (24.7 ± 1.6 Jy km s $^{-1}$; Bertram et al. 2007).⁵ Our line fluxes are reasonably consistent, with deviations $\lesssim 50\%$.

Following Solomon & Vanden Bout (2005), the CO line luminosity is

$$L'_{\text{CO}} = 3.25 \times 10^7 S_{\text{CO}} \Delta\nu \nu_{\text{obs}}^{-2} D_L^2 (1+z)^{-3}, \quad (1)$$

where L'_{CO} is the CO line luminosity in units of K km s $^{-1}$ pc 2 , $S_{\text{CO}} \Delta\nu$ is the integrated line flux in units of Jy km s $^{-1}$, ν_{obs} is the observed frequency of the CO(2–1) line in GHz, and D_L is the luminosity distance in Mpc. The factor α_{CO} is needed to derive molecular gas masses from the CO luminosity (Bolatto et al. 2013, and references therein). Since α_{CO} is usually quoted for the CO(1–0) line, we need to convert the line luminosity from $L_{\text{CO}(2-1)}$ to $L_{\text{CO}(1-0)}$ in order to derive the molecular gas mass. Fortunately, literature measurements of CO(1–0) are available for 15 of the objects in our ALMA sample, among them eight detections (Section 3.3). We find a median value of $R_{21} = 0.62^{+0.15}_{-0.07}$ (Section 4.1). We adopt this median value of R_{21} to convert all the new ALMA CO luminosities from $L_{\text{CO}(2-1)}$ to $L_{\text{CO}(1-0)}$ (Table 2). We do not consider the uncertainty on R_{21} , as it is hardly well-constrained by our data. However, if R_{21} varies from 0.5 to 1.0, it could contribute to the final uncertainty of M_{H_2} as significantly as α_{CO} (~ 0.3 dex). It is reassuring that our estimated value of R_{21} agrees well with values found in nearby galaxies and

AGNs (Ocaña Flaquer et al. 2010; Sandstrom et al. 2013; Rosolowsky et al. 2015; Husemann et al. 2017; Saintonge et al. 2017; see Section 4.1).

3.2. CO Line Width

The velocity width of the integrated emission-line profiles of galaxies is commonly specified as the line width at 20 percent (W_{20} ; e.g., Tully & Fisher 1977) or 50 percent (W_{50} ; e.g., Tiley et al. 2016) of the peak intensity. For spectra with relatively low signal-to-noise ratio, we can obtain more accurate line widths by fitting a model line profile to the data instead of measuring them directly from the observed spectrum. With the aid of a suite of integrated spectra of simulated galaxies, Tiley et al. (2016) evaluated the effectiveness of various methods for fitting line profiles and concluded that the “double-peak” Gaussian function—a parabolic function bordered by a half-Gaussian symmetrically on either side—provides the most robust measure of W_{50} . The double-peak Gaussian function is defined as (Tiley et al. 2016)

$$f(v) = \begin{cases} A_G \times \exp \frac{-(v-(v_0-w))^2}{2\sigma^2} & v < v_0 - w \\ A_C + a(v - v_0)^2 & v_0 - w \leq v \leq v_0 + w \\ A_G \times \exp \frac{-(v-(v_0+w))^2}{2\sigma^2} & v > v_0 + w \end{cases}, \quad (2)$$

where $-500 \text{ km s}^{-1} < v_0 < 500 \text{ km s}^{-1}$ is the central velocity, w ($> 0 \text{ km s}^{-1}$) is the half width of the central parabola, σ ($> 0 \text{ km s}^{-1}$) is the width of the edge half-Gaussian profile, $A_G > 0$ is the peak flux of the half-Gaussian edges at $v_0 \pm w$, A_C is the flux at the profile center, and $a = (A_G - A_C)/w^2$. Then, the two conventionally used line widths are given by

$$\begin{aligned} W_{50} &= 2(w + \sqrt{2 \ln 2} \sigma), \\ W_{20} &= 2(w + \sqrt{2 \ln 5} \sigma). \end{aligned} \quad (3)$$

Equation (3) cannot accurately specify the width of strongly convex, single-peaked profiles. Under these circumstances, the data should be fit with a standard Gaussian function,⁶ for which $W_{50} = 2\sqrt{2 \ln 2} \sigma$ and $W_{20} = 2\sqrt{2 \ln 5} \sigma$. Following Tiley et al. (2016), we adopt the standard Gaussian function when either of these two criteria holds: (1) the reduced chi-square of the standard Gaussian fit is closer to unity than that of the double-peak Gaussian function;⁷ (2) $A_G/A_C < 2/3$.

⁶ The Gaussian function is simply $f(v) = A \exp \frac{-(v-v_0)^2}{2\sigma^2}$.

⁷ The reduced χ^2 is defined as $\left(\sum_i \frac{[F(v_i) - f(v_i)]^2}{\sigma_{\text{rms}}^2} \right) / N$, where $F(v_i)$ is the observed CO(2–1) spectral flux density in velocity bin v_i , $f(v_i)$ is the model flux density, σ_{rms} is the rms noise from the line-free channels, N is the number of degrees of freedom, and the sum is taken over all of the channels.

⁵ S/T=8.19 Jy/K is assumed for the IRAM 30 m measurement.

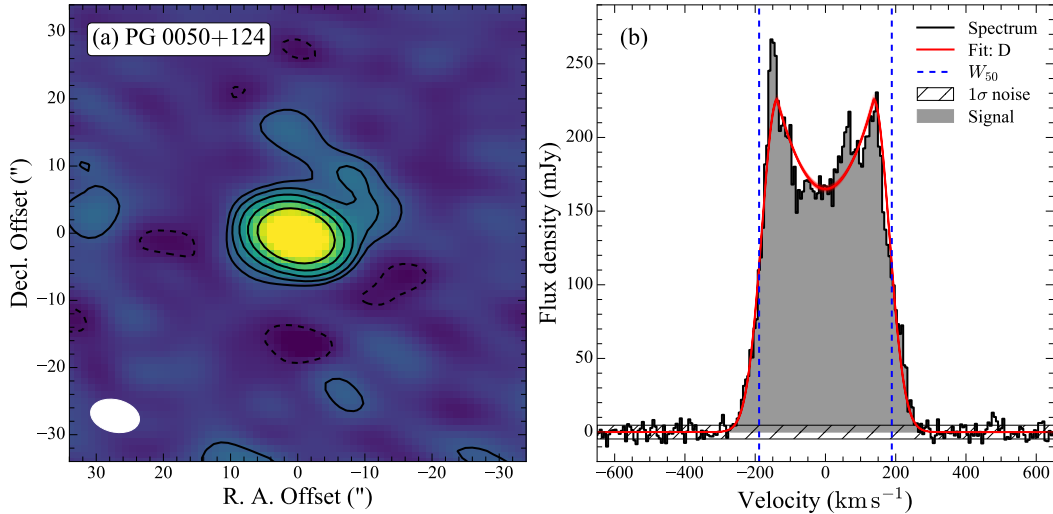


Figure 2. (a) CO(2–1) intensity (moment 0) map of PG 0050+124. The contours are -2 (dashed), 2 , 4 , 8 , 16 , and 32 σ levels, with σ being the rms of the source-free pixels in the map. The synthesis beam is indicated on the lower-left corner of the map. The beam is $7''.4 \times 4''.8$ with a position angle of 77° . (b) The one-dimensional spectrum extracted from the 2 σ contour of the source emission. Channels shaded in grey are considered to be signal from the emission line. The hatched horizontal band indicates the noise level of the line-free channels. The emission line is fit with a double-peak Gaussian profile (red curve). The full width of the 50 percentile of the best-fit profile, W_{50} , is indicated by the blue dashed lines.

We use a Markov chain Monte Carlo method in the `emcee` package (Foreman-Mackey et al. 2013) to perform the fit.

An example of the profile-fitting method is shown in Figure 2b. PG 0050+124 is one of the brightest objects in our sample. Appendix A gives the data for the remaining 20 detected objects, all of which were successfully fit, apart from the tentative detection of PG 1341+258, which suffers from exceptionally low signal-to-noise ratio. Table 2 lists measurements of both W_{50} and W_{20} , the latter because sometimes only this quantity is reported in the literature; we need to use our measured W_{20}/W_{50} ratios to incorporate the published line widths into our analysis (Section 3.3). The systemic velocities of the CO line agree closely ($< 5\%$ difference) with the optical redshifts, and for our final analysis we simply adopt the latter.

3.3. Measurements from the Literature

To date, CO(1–0) measurements have been published for 32 PG quasars, as summarized in Shangguan et al. (2018). Among them, 15 objects were included in our ALMA program and hence now have both CO transitions observed (Table 3), leaving the remaining 17 that only have CO(1–0) data (Table 4). The published CO fluxes were converted to luminosities according to our adopted cosmological parameters. Line widths were reported as either W_{20} or W_{50} , usually with no uncertainties specified. We homogenize the line widths adopting $W_{20}/W_{50} = 1.17 \pm 0.19$, the median ratio measured in

our ALMA sample. Of the 15 quasars with both CO(1–0) and CO(2–1) observations, eight are detected in both lines.⁸ These objects provide valuable insight on R_{21} (Section 4.1), which is needed to convert the line luminosity from CO(2–1) to CO(1–0), as discussed in Section 3.1.

4. DISCUSSION

4.1. The CO(2–1)/CO(1–0) Ratio

As listed in Table 3, the line ratios of the eight quasars in our study with both lines detected span $R_{21} = 0.49 - 0.90$. The 50^{+25}_{-25} th percentile value, calculated with the Kaplan-Meier product-limit estimator `kestimate` in `IRAF.ASURV` (Feigelson & Nelson 1985; Lavalley et al. 1992), is $R_{21} = 0.62^{+0.15}_{-0.07}$. If the CO emission is thermalized and optically thick, the intrinsic brightness temperature and luminosity of the line are independent of J and rest frequency, and $R_{21} = 1$. Indeed, a value of $R_{21} \approx 1$ is observed in the inner parts of spiral galaxies (Braine & Combes 1992), local luminous IR galaxies (Papadopoulos et al. 2012), and high-redshift galaxies (Carilli & Walter 2013; Daddi et al. 2015). However, recent studies find lower values of R_{21} on the global scales of nearby galactic disks ($R_{21} \lesssim 0.8$;

⁸ According to Shangguan et al. (2018), the 3 σ CO(1–0) detections of PG 0003+199 (Maiolino et al. 1997) and PG 2214+139 (Scoville et al. 2003) were likely overestimated. We regard them as upper limits.

Leroy et al. 2013; Rosolowsky et al. 2015; Saintonge et al. 2017). Ocaña Flaquer et al. (2010) report $R_{21} \approx 0.6$ for nearby radio galaxies, and some low-redshift quasars can reach $R_{21} \approx 0.5$ (Husemann et al. 2017), while in IR-luminous quasars $R_{21} \approx 0.4 - 1.2$, with a mean value of ~ 0.8 (Xia et al. 2012). Therefore, our low-redshift quasars exhibit R_{21} values fully consistent with those derived from global measurements of nearby inactive and active galaxies. In contrast, high-redshift quasars show low- J CO line ratios suggestive of optically thick, thermally excited emission, indicating that the molecular gas emission comes from a compact region in the centers of the host galaxies (Carilli & Walter 2013).

The relative spatial coverage of CO(1–0) and CO(2–1) introduces additional uncertainties into the interpretation of R_{21} , especially for single-beam observations of nearby galaxies when both lines are observed with the same telescope⁹ or interferometer configuration. To alleviate such complications, it is customary to scale down the flux of CO(1–0) to match that of CO(2–1), often limiting the measurement of the line ratio to the central part of the galaxy. For example, Husemann et al. (2017) use H α emission to estimate the spatial distribution of CO(1–0) and scale down the flux of CO(1–0) to match that of CO(2–1). Saintonge et al. (2017), in contrast, observe CO(2–1) using the APEX 12 m telescope, whose 230 GHz beam of $27''$ better matches the $22''$ beam of the IRAM 30 m telescope for CO(1–0). Fortunately, the relatively large distances of our sources obviate these complications. At $z \gtrsim 0.05$, the CO(1–0) emission of our objects should be mostly captured by the beam of the IRAM 30 m telescope (Evans et al. 2006; Bertram et al. 2007), while all of the CO(2–1) emission should be contained within the maximum recoverable scale ($\sim 29''$ at 230 GHz) of ACA, which is confirmed by our $15''$ tapered measurements (Section 2). Meanwhile, CO(1–0) emission may still be underestimated to some extent, when the emission size is comparable to the beam size but its spatial distribution is unknown from the single-dish observation. This may also contribute to the uncertainty of R_{21} .

The low values of R_{21} for our quasars indicate that the molecular gas is optically thick but either is subthermally excited (Ocaña Flaquer et al. 2010; Husemann et al. 2017) or has low temperature ($\lesssim 10$ K; Braine & Combes 1992). Motivated by Daddi et al. (2015), who found a significant sublinear correlation between the mean intensity of the interstellar radiation field of the galaxy ($\langle U \rangle$; Draine & Li 2007) and the

CO(5–4)/CO(2–1) ratio, we checked but failed to find a clear correlation between R_{21} and $\langle U \rangle$ for the quasar host galaxies (Figure 3a). Unfortunately, the number of objects with statistically meaningful measurements is too small to perform a formal statistical test. $\langle U \rangle$ comes from the study of IR spectral energy distributions of PG quasars (Shangguan et al. 2018). The dust temperatures of the quasar host galaxies, however, are $\gtrsim 20$ K (Shangguan et al. 2018), which are not entirely consistent with the molecular gas temperature of $\lesssim 10$ K expected from $R_{21} \approx 0.6$, if the gas is thermally excited (see Figure 1 of Braine & Combes 1992). Although a detailed discussion is beyond the scope of this paper, we note that the continuum emission of almost all of the quasars are unresolved with our ACA measurements, while CO(2–1) of nearly half of the quasars is resolved.¹⁰ This suggests that the dust emission from far-IR to submillimeter is predominantly powered by an AGN or nuclear starburst. We do not know whether the quasar affects the excitation of the low- J CO lines, as R_{21} seems unrelated to the AGN luminosity (Figure 3b). We conclude that, similar as low- z galaxies and AGNs, the low- J CO emission of our quasars is subthermally excited.

4.2. IR versus CO Relation

The CO line luminosity correlates strongly with the IR luminosity of galaxies, both active and inactive, at low and high redshifts (e.g., Sanders & Mirabel 1985; Solomon & Vanden Bout 2005; Genzel et al. 2010; Saintonge et al. 2011b; Xia et al. 2012; Carilli & Walter 2013). Sensitive to the Lyman continuum emission absorbed and reprocessed by dust (Kennicutt 1998b), the IR luminosity provides an excellent tracer of the star formation rate in star-forming galaxies. Therefore, the ratio of L_{IR} to $L'_{\text{CO}(1-0)}$ reflects the global star formation efficiency of the molecular gas. In quasar host galaxies, however, emission from hot dust, heated by BH accretion, may dominate the IR luminosity and contribute a significant fraction of the emission, even up to $\sim 100 \mu\text{m}$ (Lani et al. 2017; Lyu & Rieke 2017; Zhuang et al. 2018). We calculate the 8–1000 μm IR luminosity from the cold dust emission decomposed from the integrated spectral energy distributions of Shangguan et al. (2018).¹¹

Figure 4 compares the $L_{\text{IR}}-L'_{\text{CO}(1-0)}$ relation of PG quasars with those of star-forming galaxies and starburst systems triggered by galaxy mergers (Genzel et al. 2010). Starburst galaxies are typically $\gtrsim 0.4$ dex above the so-called main sequence of the star-forming galax-

¹⁰ The size measurements are based on CASA 2D fit.

¹¹ We adopt the quantity $L_{\text{IR,host}}$ from Shangguan et al. (2018), but denote it here as L_{IR} for short.

⁹ The IRAM 30 m beam size is $22''$ for CO(1–0) and $11''$ for CO(2–1).

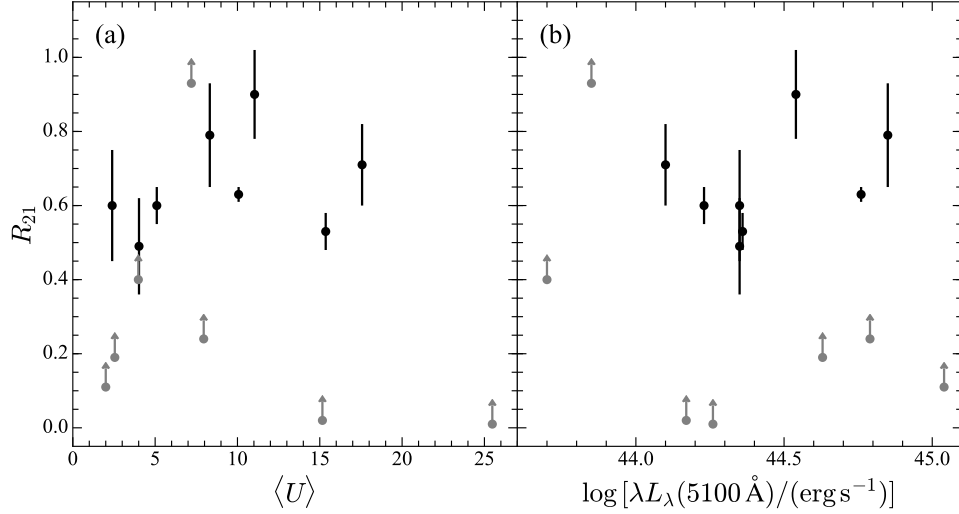


Figure 3. The relation between CO line intensity ratio R_{21} and (a) the mean intensity of the interstellar radiation field $\langle U \rangle$ and (b) quasar 5100 Å continuum luminosity. Objects with CO(1–0) upper limits are denoted as grey symbols. A possible increasing trend is found in (a), but none is obvious in (b).

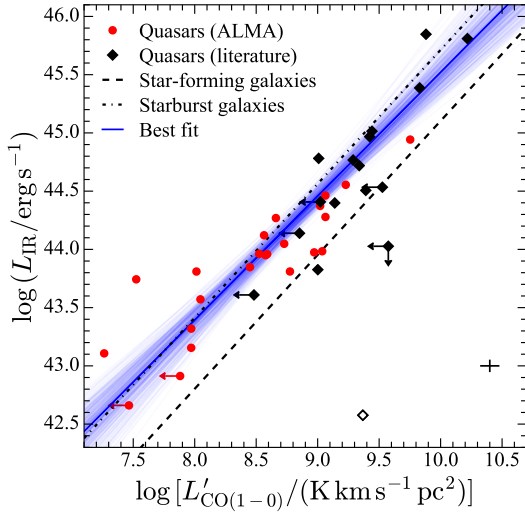


Figure 4. The relation between IR and CO luminosity for quasar host galaxies, compared with those of normal star-forming galaxies (dashed line) and nearby and high-redshift starburst galaxies (dash-dotted line) from Genzel et al. (2010). The blue solid line is the best-fit relation for quasars, including the upper limits of $L'_{\text{CO}(1-0)}$. The faint blue lines indicate the uncertainty of the fit. The 90th percentiles of the measured uncertainties are indicated in the lower-right corner. We exclude PG 1226+023 (open diamond) from the fit, as the IR luminosity of its host galaxy is very uncertain.

ies (e.g., Elbaz et al. 2018; Shangguan et al. 2019a). As with other types of galaxies, the host galaxies of quasars

clearly also exhibit a strong correlation. We fit the re-

lation of the PG quasars with *Linmix* (Kelly 2007),¹² accounting for the upper limits in $L'_{\text{CO}(1-0)}$. The best fit,

$$\log L'_{\text{CO}(1-0)} = 0.94 \left({}^{+0.08}_{-0.08} \right) \log L_{\text{IR}} - 32.90 \left({}^{+3.35}_{-3.40} \right), \quad (4)$$

is consistent with a linear relation between L_{IR} and $L'_{\text{CO}(1-0)}$. Both the slope and the zero point are consistent with the relation for starburst galaxies. The total scatter of the relation (~ 0.3 dex) is dominated by an intrinsic scatter of $0.29^{+0.05}_{-0.04}$ dex. PG 1226+023 is excluded from the fit because the IR luminosity of its host galaxy is very uncertain (see Table 4 and Shangguan et al. 2018), but the fit results do not depend on this choice. We searched for, but failed to find, a statistically significant partial correlation of the $L_{\text{IR}}-L'_{\text{CO}(1-0)}$ relation with any plausible third variable (e.g., AGN luminosity).

4.3. CO-to-H₂ Conversion Factor

To the best of our knowledge, there has never been a formal study of the CO-to-H₂ conversion factor (α_{CO})

¹² Since *Linmix* only allows upper limits on the dependent variable, we treat L_{IR} as the independent variable and $L'_{\text{CO}(1-0)}$ as the dependent variable. We do not include PG 1545+210, which contains upper limits in both L_{IR} and $L'_{\text{CO}(1-0)}$. We assign an uncertainty of 0.1 dex to the literature measurements for which error estimates are unavailable, but the exact value is not critical to the fit.

of galaxies hosting AGNs powerful enough to qualify as quasars. Here we use our new CO measurements, in combination with previous total gas measurements estimated from dust content (Shangguan et al. 2018), to put a rough constraint on α_{CO} in quasar host galaxies. As a starting point, we adopt $\alpha_{\text{CO}} = 3.1 M_{\odot} (\text{K km s}^{-1} \text{pc}^2)^{-1}$ with 0.3 dex uncertainty, as recommended by Sandstrom et al. (2013), who, as in Leroy et al. (2011), simultaneously solved for α_{CO} and the gas-to-dust ratio for 26 nearby star-forming galaxies, for the first time beyond the Local Group. This value of α_{CO} is slightly lower than, but consistent with, the canonical Milky Way value of $4.3 M_{\odot} (\text{K km s}^{-1} \text{pc}^2)^{-1}$ (Bolatto et al. 2013), and it does not appear to depend strongly on metallicity for galaxies with metallicities similar to and above that of the Milky Way. While nuclear activity potentially can affect the molecular gas of the host (e.g., Krips et al. 2008), there is no clear evidence that the presence of an AGN influences α_{CO} (Sandstrom et al. 2013), even when AGN feedback is in principle powerful enough to be effective (Rosario et al. 2018).

Figure 5 plots the variation of the molecular gas fraction ($M_{\text{H}_2}/M_{\text{gas}}$) as a function of stellar mass (M_{\star}), where M_{gas} is the total mass of the cold interstellar medium ($M_{\text{HI}} + M_{\text{H}_2}$) inferred from the dust mass, as described in Shangguan et al. (2018). The host galaxies of PG quasars,¹³ accounting for the censored data, have a 50 ± 25 percentile molecular gas fraction of $40\% \pm 24\%$ and a stellar mass of $10^{10.89 \pm 0.22} M_{\odot}$.¹⁴ The quasars gathered from the literature on average have a higher molecular gas fraction than those newly observed using ALMA. This is an obvious observational selection effect. If we limit ourselves to the unbiased ALMA sample, the 50 ± 25 percentile molecular gas fraction becomes $32\% \pm 18\%$ for a stellar mass of $10^{10.86 \pm 0.19} M_{\odot}$. The molecular gas fraction of the quasars are in rough agreement with, but slightly more elevated than, that of inactive galaxies of similar stellar mass (Catinella et al. 2018; blue line in Figure 5).¹⁵ This is not unexpected. AGNs in general and quasars in particular reside preferentially in bulge-dominated galaxies (Ho et al. 1997; Ho 2008; Kim et al. 2017; Zhao et al. 2019), and bulge-dominated systems tend to have higher molecular gas

fractions (Catinella et al. 2018). In other words, at any given stellar mass, AGN hosts, by virtue of their earlier type morphologies, should have higher molecular gas fractions, as observed.

The above analysis, while far from a rigorous derivation, does suggest that the host galaxies of low-redshift quasars have an α_{CO} value not too dissimilar from that of ordinary star-forming galaxies and lower luminosity AGNs. We do not believe that the CO-to-H₂ conversion factor of PG quasars can be as low as $\alpha_{\text{CO}} = 0.8 M_{\odot} (\text{K km s}^{-1} \text{pc}^2)^{-1}$, a value commonly advocated for ultraluminous IR galaxies (ULIRGs; Downes & Solomon 1998). Such a low value of α_{CO} would result in molecular gas mass fractions substantially lower than those of star-forming galaxies (orange pentagon in Figure 5). This seems improbable. As shown in Section 4.2, quasar host galaxies follow nearly the same $L_{\text{IR}}-L'_{\text{CO}(1-0)}$ relation as starburst galaxies, suggesting that they have similarly high star formation efficiencies.

5. SUMMARY

We present new ALMA Compact Array observations of the CO(2–1) line for 23 $z < 0.1$ Palomar-Green quasars. We detect CO(2–1) emission in 21 objects—13 for the first time—and provide stringent upper limits for the remaining two, almost doubling the number of PG quasars with CO detections. Combined with published CO(1–0) observations, we assemble CO measurements for a representative sample of 40 $z < 0.3$ PG quasars, which forms the basis of a companion investigation on the relations between AGN properties and the molecular gas properties of quasar host galaxies (Shangguan et al. 2019b).

This work, primarily devoted to the observational aspects of the new ALMA observations and the general characteristics of the sample, highlights the following results:

- The CO(2–1)/CO(1–0) ratio of low-redshift quasar host galaxies, $R_{21} = 0.62^{+0.15}_{-0.07}$, is broadly consistent with that of low-redshift star-forming and active galaxies. The molecular gas is likely subthermal. We do not find a strong correlation between R_{21} and the mean intensity of the interstellar radiation field or AGN luminosity.
- Quasar host galaxies follow a tight, linear $L_{\text{IR}}-L'_{\text{CO}(1-0)}$ relation that strongly resembles the behavior of starburst galaxies.
- Quasar host galaxies have molecular-to-total gas mass fractions slightly higher than, but generally consistent with, those of normal galaxies, if the

¹³ For the purposes of this discussion, we exclude PG 1545+210, whose molecular gas mass and total gas mass are upper limits.

¹⁴ Again, PG 1226+023 is excluded because its total gas mass, derived from the dust mass, is very uncertain (see Table 4 and Shangguan et al. 2018). However, the median values are barely affected by this choice.

¹⁵ Catinella et al. (2018) used a variable α_{CO} , which is on average $\sim 3.0 M_{\odot} (\text{K km s}^{-1} \text{pc}^2)^{-1}$ for galaxies with $M_{\star} > 10^{10.5} M_{\odot}$, very close to our value.

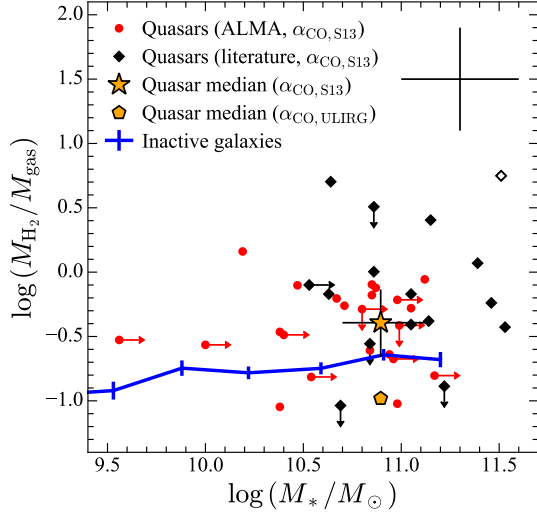


Figure 5. The molecular-to-total gas mass ratios of quasars are consistent with those of inactive galaxies, within the scatter. The total gas mass is estimated from the dust mass (Shangguan et al. 2018). The relation between $M_{\text{H}_2}/M_{\text{gas}}$ and stellar mass for inactive galaxies (blue line) is derived from Catinella et al. (2018). The median and ± 25 th percentiles of $M_{\text{H}_2}/M_{\text{gas}}$ and M_* for the quasars, accounting for the censored data, are shown as the orange star, where we have assumed the CO-to- H_2 conversion factor of star-forming galaxies from Sandstrom et al. (2013, $\alpha_{\text{CO},\text{S13}} = 3.1 M_{\odot} (\text{K km s}^{-1} \text{pc}^2)^{-1}$). The median gas mass ratio calculated assuming a conversion factor appropriate for ULIRGs (orange pentagon; $\alpha_{\text{CO},\text{ULIRG}} = 0.8 M_{\odot} (\text{K km s}^{-1} \text{pc}^2)^{-1}$) is significantly lower than that for inactive galaxies. We exclude PG 1226+023 (open diamond) in calculating the median values, as its total gas mass is very uncertain. The uncertainties of the x-axis (~ 0.3 dex) and y-axis (~ 0.4 dex) are indicated in the upper-right corner.

CO-to- H_2 conversion factor is that of nearby star-forming galaxies, $\alpha_{\text{CO}} = 3.1 M_{\odot} (\text{K km s}^{-1} \text{pc}^2)^{-1}$.

APPENDIX

A. CO(2–1) MEASUREMENTS FOR INDIVIDUAL OBJECTS

We detected CO(2–1) emission in 21 out of 23 PG quasars. Figure 6 shows the moment 0 maps and one-dimensional spectra for 20 objects; the data for PG 0050+124 appear in Figure 2. The signal-to-noise ratio of PG 1341+258 is too low to robustly fit its line profile. We believe PG 1341+258 is marginally detected, because we always detect the source with $\sim 4\sigma$ significance when we clean the data with different velocity channel widths.

REFERENCES

- Astropy Collaboration, Robitaille, T. P., Tollerud, E. J., et al. 2013, *A&A*, 558, A33
- Baron, D., Netzer, H., Prochaska, J. X., et al. 2018, *MNRAS*, 480, 3993
- Bertram, T., Eckart, A., Fischer, S., et al. 2007, *A&A*, 470, 571
- Bigiel, F., Leroy, A., Walter, F., et al. 2008, *AJ*, 136, 2846

We are grateful to an anonymous referee for helpful comments and suggestions. We acknowledge support from: the National Science Foundation of China grant 11721303 (LCH), the National Key R&D Program of China grant 2016YFA0400702 (LCH); CONICYT-Chile grants Basal AFB-170002 (FEB, ET), FONDO ALMA 31160033 (FEB), FONDECYT Regular 1160999 (ET) and 1190818 (ET, FEB), and Anillo de ciencia y tecnologia ACT1720033 (ET); and the Chilean Ministry of Economy, Development, and Tourism's Millennium Science Initiative through grant IC120009, awarded to The Millennium Institute of Astrophysics, MAS (FEB). JS thanks Feng Long, Jiayi Sun, Ming-Yang Zhuang, Yali Shao, and Jianan Li for helpful discussions. He is also grateful to Yulin Zhao for sharing the GALFIT results of the PG quasar host galaxies. Hassen Yusef provided valuable advice on statistical methods. This paper makes use of the following ALMA data: ADS/JAO.ALMA#2017.1.00297.S. ALMA is a partnership of ESO (representing its member states), NSF (USA) and NINS (Japan), together with NRC (Canada), MOST and ASIAA (Taiwan), and KASI (Republic of Korea), in cooperation with the Republic of Chile. The Joint ALMA Observatory is operated by ESO, AUI/NRAO and NAOJ.

Facilities: ALMA

Software: CASA (McMullin et al. 2007), astropy (Astropy Collaboration et al. 2013), PyRAF¹⁶

¹⁶ PyRAF is a product of the Space Telescope Science Institute, which is operated by AURA for NASA.

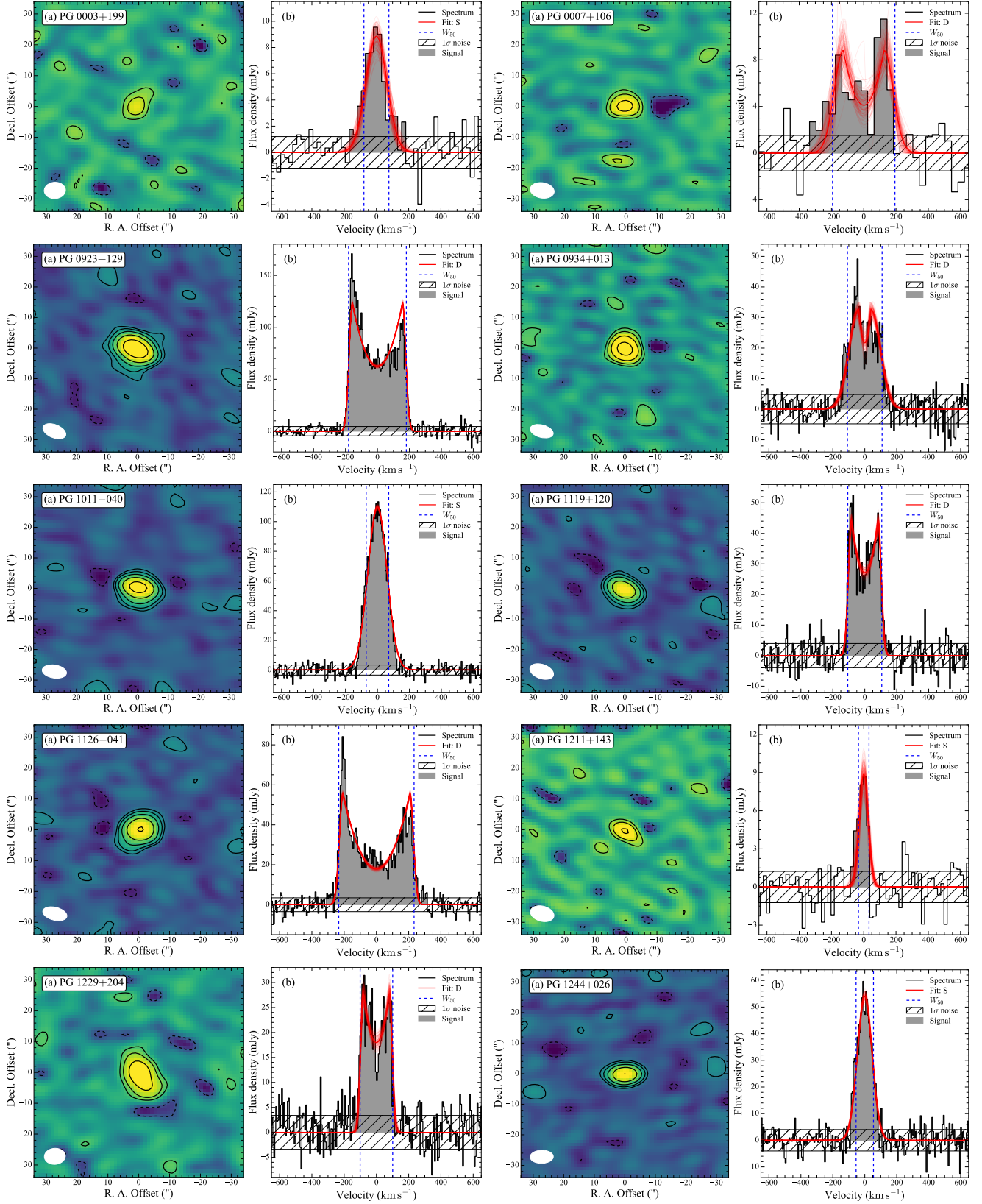


Figure 6. Objects in the survey detected in CO(2–1). (a) Intensity (moment 0) map. The contours are -2 (dashed), 2 , 4 , 8 , 16 , and 32σ levels, with σ being the rms of the source-free pixels in the map. The synthesis beam is indicated on the lower-left corner of the map. (b) The one-dimensional spectrum extracted from the 2σ contour of the source emission. Channels shaded in grey are considered to be signal from the emission line. The hatched horizontal band indicates the noise level of the line-free channels. The best-fit emission-line profile is plotted with a red curve, with the uncertainty displayed with faint thin red lines. The double-peaked Gaussian profile is indicated with “Fit: D”, while the single Gaussian profile is indicated with “Fit: S”. The full width of the 50 percentile of the best-fit profile, W_{50} , is indicated by the blue dashed lines.

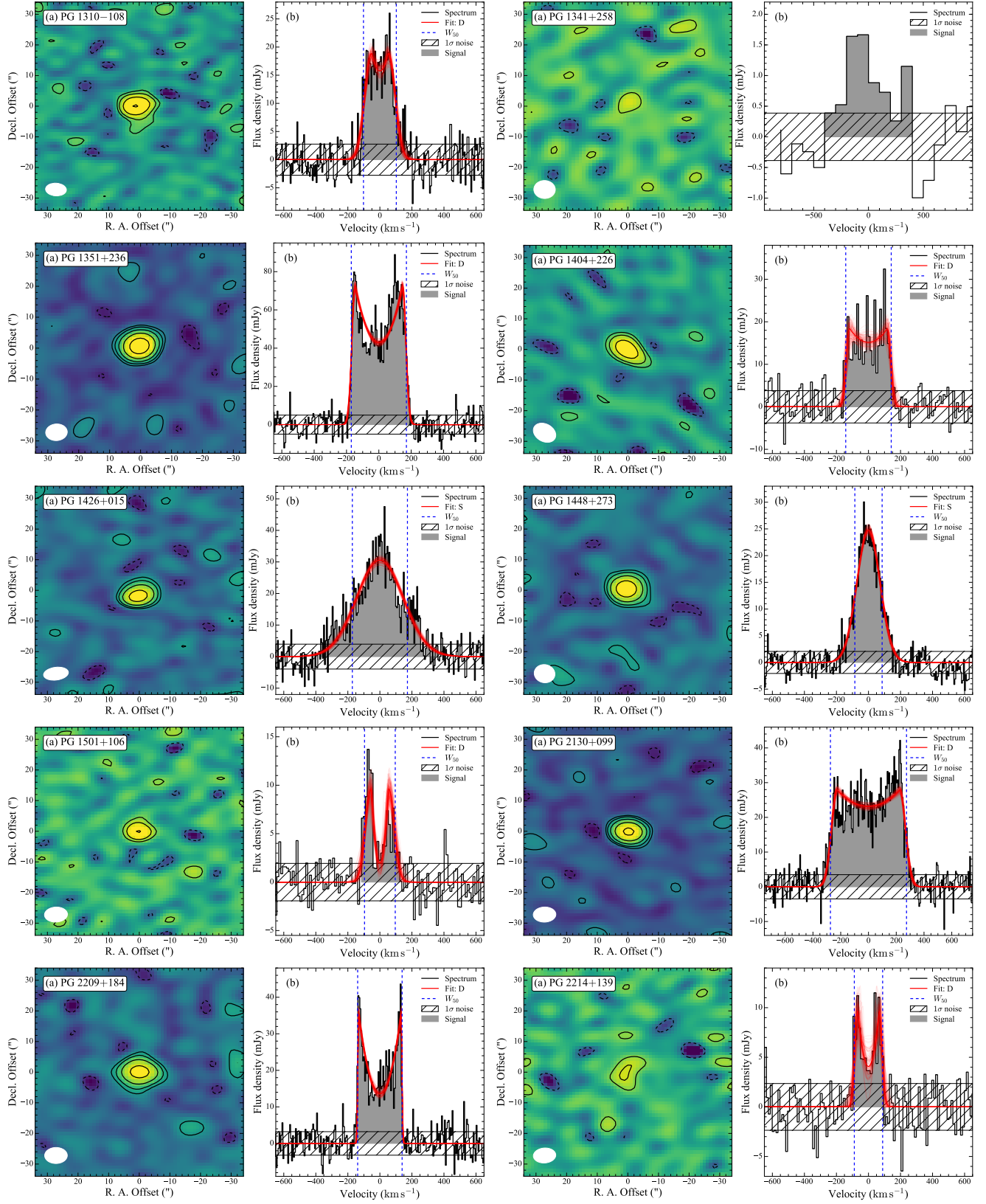


Figure 6. Continued.

- Bischetti, M., Maiolino, R., Carniani, S., et al. 2019, A&A, in press (arXiv:1806.00786)
- Bischetti, M., Piconcelli, E., Vietri, G., et al. 2017, A&A, 598, A122
- Bolatto, A. D., Wolfire, M., & Leroy, A. K. 2013, ARA&A, 51, 207
- Bonato, M., Liuzzo, E., Giannetti, A., et al. 2018, MNRAS, 478, 1512
- Bonfield, D. G., Jarvis, M. J., Hardcastle, M. J., et al. 2011, MNRAS, 416, 13
- Borson, T. A., & Green, R. F. 1992, ApJS, 80, 109
- Braine, J., & Combes, F. 1992, A&A, 264, 433
- Brusa, M., Cresci, G., Daddi, E., et al. 2018, A&A, 612, A29
- Cano-Díaz, M., Maiolino, R., Marconi, A., et al. 2012, A&A, 537, L8
- Carilli, C. L., & Walter, F. 2013, ARA&A, 51, 105
- Carniani, S., Marconi, A., Maiolino, R., et al. 2016, A&A, 591, A28
- Casoli, F., & Loinard, L. 2001, Science with the Atacama Large Millimeter Array, 305
- Catinella, B., Saintonge, A., Janowiecki, S., et al. 2018, MNRAS, 476, 875
- Catinella, B., Schiminovich, D., Kauffmann, G., et al. 2010, MNRAS, 403, 683
- Cicone, C., Maiolino, R., Sturm, E., et al. 2014, A&A, 562, A21
- Combes, F., García-Burillo, S., Audibert, A., et al. 2019, A&A, 623, A79
- Cresci, G., Mainieri, V., Brusa, M., et al. 2015, ApJ, 799, 82
- Daddi, E., Dannerbauer, H., Liu, D., et al. 2015, A&A, 577, A46
- Daddi, E., Dickinson, M., Morrison, G., et al. 2007, ApJ, 670, 156
- Daddi, E., Elbaz, D., Walter, F., et al. 2010, ApJ, 714, L118
- Dai, Y. S., Wilkes, B. J., Bergeron, J., et al. 2018, MNRAS, 478, 4238
- Diamond-Stanic, A. M., & Rieke, G. H. 2012, ApJ, 746, 168
- Di Matteo, T., Springel, V., & Hernquist, L. 2005, Nature, 433, 604
- Downes, D., & Solomon, P. M. 1998, ApJ, 507, 615
- Draine, B. T., & Li, A. 2007, ApJ, 657, 810
- Elbaz, D., Leiton, R., Nagar, N., et al. 2018, A&A, 616, A110
- Ellison, S. L., Catinella, B., & Cortese, L. 2018, MNRAS, 478, 3447
- Esquej, P., Alonso-Herrero, A., González-Martín, O., et al. 2014, ApJ, 780, 86
- Evans, A. S., Frayer, D. T., Surace, J. A., et al. 2001, AJ, 121, 1893
- Evans, A. S., Hines, D. C., Barthel, P., et al. 2009, AJ, 138, 262
- Evans, A. S., Solomon, P. M., Tacconi, L. J., et al. 2006, AJ, 132, 2398
- Fabian, A. C. 2012, ARA&A, 50, 455
- Feigelson, E. D., & Nelson, P. I. 1985, ApJ, 293, 192
- Feruglio, C., Fiore, F., Carniani, S., et al. 2015, A&A, 583, A99
- Fomalont, E., van Kempen, T., Kneissl, R., et al. 2014, The Messenger, 155, 19
- Foreman-Mackey, D., Hogg, D. W., Lang, D., et al. 2013, PASP, 125, 306
- García-Burillo, S., & Combes, F. 2012, Journal of Physics Conference Series, 012050
- Genzel, R., Tacconi, L. J., Gracia-Carpio, J., et al. 2010, MNRAS, 407, 2091
- Harrison, C. M., Costa, T., Tadhunter, C. N., et al. 2018, Nature Astronomy, 2, 198
- Heckman, T. M., & Best, P. N. 2014, ARA&A, 52, 589
- Herrera-Camus, R., Tacconi, L., Genzel, R., et al. 2019, ApJ, 871, 37
- Hirschmann, M., Somerville, R. S., Naab, T., et al. 2012, MNRAS, 426, 237
- Ho, L. C. 2008, ARA&A, 46, 475
- Ho, L. C., Darling, J., & Greene, J. E. 2008, ApJ, 681, 128
- Ho, L. C., Filippenko, A. V., & Sargent, W. L. W. 1997, ApJ, 487, 568
- Hong, J., Im, M., Kim, M., et al. 2015, ApJ, 804, 34
- Hopkins, P. F., Hernquist, L., Cox, T. J., & Kereš, D. 2008, ApJS, 175, 356
- Husemann, B., Bennert, V. N., Jahnke, K., et al. 2019, ApJ, 879, 75
- Husemann, B., Davis, T. A., Jahnke, K., et al. 2017, MNRAS, 470, 1570
- Isobe, T., Feigelson, E. D., & Nelson, P. I. 1986, ApJ, 306, 490
- Izumi, T. 2018, PASJ, 70, L2
- Izumi, T., Kawakatu, N., & Kohno, K. 2016, ApJ, 827, 81
- Kelly, B. C. 2007, ApJ, 665, 1489
- Kennicutt Jr., R. C. 1998a, ApJ, 498, 541
- Kennicutt, R. C. 1998b, ARA&A, 36, 189
- Kim, M., Ho, L. C., Peng, C. Y., et al. 2017, ApJS, 232, 21
- Kormendy, J., & Ho, L. C. 2013, ARA&A, 51, 511
- Krips, M., Neri, R., García-Burillo, S., et al. 2008, ApJ, 677, 262
- Lani, C., Netzer, H., & Lutz, D. 2017, MNRAS, 471, 59
- Lavalley, M., Isobe, T., & Feigelson, E. 1992, Astronomical Data Analysis Software and Systems I, 245
- Leroy, A. K., Bolatto, A., Gordon, K., et al. 2011, ApJ, 737, 12

- Leroy, A. K., Walter, F., Sandstrom, K., et al. 2013, *AJ*, 146, 19
- Lutz, D., Shimizu, T., Davies, R. I., et al. 2018, *A&A*, 609, A9
- Lyu, J., & Rieke, G. H. 2017, *ApJ*, 841, 76
- Maiolino, R., Gallerani, S., Neri, R., et al. 2012, *MNRAS*, 425, L66
- Maiolino, R., Ruiz, M., Rieke, G. H., et al. 1997, *ApJ*, 485, 552
- McLure, R. J., & Dunlop, J. S. 2004, *MNRAS*, 352, 1390
- McMullin, J. P., Waters, B., Schiebel, D., et al. 2007, *Astronomical Data Analysis Software and Systems XVI*, 127
- Noeske, K. G., Weiner, B. J., Faber, S. M., et al. 2007, *ApJ*, 660, L43
- Ocaña Flaquer, B., Leon, S., Combes, F., et al. 2010, *A&A*, 518, A9
- Papadopoulos, P. P., Kovacs, A., Evans, A. S., et al. 2008, *A&A*, 491, 483
- Papadopoulos, P. P., van der Werf, P. P., Xilouris, E. M., et al. 2012, *MNRAS*, 426, 2601
- Peng, C. Y., Ho, L. C., Impey, C. D., & Rix, H.-W. 2002, *AJ*, 124, 266
- Peng, C. Y., Ho, L. C., Impey, C. D., & Rix, H.-W. 2010, *AJ*, 139, 2097
- Perna, M., Sargent, M. T., Brusa, M., et al. 2018, *A&A*, 619, A90
- Planck Collaboration, Ade, P. A. R., Aghanim, N., et al. 2016, *A&A*, 594, A13
- Richards, G. T., Lacy, M., Storrie-Lombardi, L. J., et al. 2006, *ApJS*, 166, 470
- Rosario, D. J., Burtscher, L., Davies, R. I., et al. 2018, *MNRAS*, 473, 5658
- Rosolowsky, E., Leroy, A. K., Usero, A., et al. 2015, *BAAS*, 225, 141.25
- Russell, H. R., McNamara, B. R., Fabian, A. C., et al. 2019, *MNRAS*, in press (arXiv:1902.09227)
- Saintonge, A., Catinella, B., Tacconi, L. J., et al. 2017, *ApJS*, 233, 22
- Saintonge, A., Kauffmann, G., Kramer, C., et al. 2011, *MNRAS*, 415, 32
- Saintonge, A., Kauffmann, G., Wang, J., et al. 2011, *MNRAS*, 415, 61
- Sanders, D. B., & Mirabel, I. F. 1985, *ApJ*, 298, L31
- Sandstrom, K. M., Leroy, A. K., Walter, F., et al. 2013, *ApJ*, 777, 5
- Sargent, M. T., Daddi, E., Béthermin, M., et al. 2014, *ApJ*, 793, 19
- Schmidt, M., & Green, R. F. 1983, *ApJ*, 269, 352
- Scoville, N. Z., Frayer, D. T., Schinnerer, E., et al. 2003, *ApJ*, 585, L105
- Scoville, N., Sheth, K., Aussel, H., et al. 2016, *ApJ*, 820, 83
- Shangguan, J., & Ho, L. C. 2019, *ApJ*, 873, 90
- Shangguan, J., Ho, L. C., Li, R., et al. 2019a, *ApJ*, 870, 104
- Shangguan, J., Ho, L. C., Bauer, F. E., Wang, R., & Treister, E. 2019b, *ApJ*, submitted
- Shangguan, J., Ho, L. C., & Xie, Y. 2018, *ApJ*, 854, 158
- Shao, Y., Wang, R., Jones, G. C., et al. 2017, *ApJ*, 845, 138
- Solomon, P. M., & Vanden Bout, P. A. 2005, *ARA&A*, 43, 677
- Storchi-Bergmann, T., & Schnorr-Müller, A. 2019, *Nature Astronomy*, 3, 48
- Strong, A. W., & Mattox, J. R. 1996, *A&A*, 308, L21
- Tacconi, L. J., Genzel, R., Saintonge, A., et al. 2018, *ApJ*, 853, 179
- Tan, Q.-H., Gao, Y., Kohno, K., et al. 2019, arXiv e-prints, arXiv:1910.10360
- Tiley, A. L., Bureau, M., Saintonge, A., et al. 2016, *MNRAS*, 461, 3494
- Topal, S., Bureau, M., Tiley, A. L., et al. 2018, *MNRAS*, 479, 3319
- Tully, R. B., & Fisher, J. R. 1977, *A&A*, 500, 105
- Vayner, A., Wright, S. A., Murray, N., et al. 2017, *ApJ*, 851, 126
- Vestergaard, M., & Peterson, B. M. 2006, *ApJ*, 641, 689
- Walter, F., Carilli, C., Bertoldi, F., et al. 2004, *ApJ*, 615, L17
- Wang, R., Wagg, J., Carilli, C. L., et al. 2013, *ApJ*, 773, 44
- Wang, R., Wu, X.-B., Neri, R., et al. 2016, *ApJ*, 830, 53
- Westmeier, T., Jurek, R., Obreschkow, D., Koribalski, B. S., & Staveley-Smith, L. 2014, *MNRAS*, 438, 1176
- Xia, X. Y., Gao, Y., Hao, C.-N., et al. 2012, *ApJ*, 750, 92
- Xu, L., Rieke, G. H., Egami, E., et al. 2015, *ApJ*, 808, 159.
- Zhang, Z., Shi, Y., Rieke, G. H., et al. 2016, *ApJ*, 819, L27
- Zhao, D., Ho, L. C., Zhao, Y., et al. 2019, *ApJ*, 877, 52
- Zhuang, M.-Y., Ho, L. C., & Shangguan, J. 2018, *ApJ*, 862, 118
- Zhuang, M.-Y., Ho, L. C., & Shangguan, J. 2019, *ApJ*, 873, 103 (erratum: 2019, *ApJ*, 875, 78)

Table 1. PG Quasars ALMA Observations

Object	z	R.A.	Decl.	Flux & Bandpass	Phase	PWV	T_{int}
		(J2000.0)	(J2000.0)	Calibrator	Calibrator	(mm)	(minute)
(1)	(2)	(3)	(4)	(5)	(6)	(7)	(8)
PG 0003+199	0.025	00:06:19.52	+20:12:10.5	J2253+1608	J0019+2021	0.769 ± 0.166	150.58
PG 0007+106	0.089	00:10:31.01	+10:58:29.5	J2253+1608	J0010+1724/J0022+0608	2.314 ± 0.108	150.69
PG 0049+171	0.064	00:51:54.80	+17:25:58.4	J2253+1608	J0019+2021	1.222 ± 0.100	152.27
PG 0050+124	0.061	00:53:34.94	+12:41:36.2	J2253+1608	J0121+1149	1.079 ± 0.118	152.16
PG 0923+129	0.029	09:26:03.29	+12:44:03.6	J0522-3627/J1058+0133	J0854+2006	1.353 ± 0.011	152.22
PG 0934+013	0.050	09:37:01.03	+01:05:43.5	J1058+0133/J0854+2006	J0948+0022	0.506 ± 0.020	149.05
PG 1011-040	0.058	10:14:20.69	-04:18:40.5	J1058+0133	J1010-0200/J0942-0759	0.656 ± 0.004	151.13
PG 1119+120	0.049	11:21:47.10	+11:44:18.3	J1058+0133	J1116+0829	1.233 ± 0.024	149.00
PG 1126-041	0.060	11:29:16.66	-04:24:07.6	J1058+0133	J1131-0500	0.720 ± 0.069	150.63
PG 1211+143	0.085	12:14:17.70	+14:03:12.6	J1229+0203	J1215+1654	2.268 ± 0.067	150.65
PG 1229+204	0.064	12:32:03.60	+20:09:29.2	J1229+0203	J1224+2122	3.089 ± 0.112	149.25
PG 1244+026	0.048	12:46:35.25	+02:22:08.8	J1256-0547/J1058+0133	J1229+0203	0.839 ± 0.018	148.98
PG 1310-108	0.035	13:13:05.78	-11:07:42.4	J1256-0547/J1337-1257	J1337-1257/J1256-0547	0.471 ± 0.092	150.81
PG 1341+258	0.087	13:43:56.75	+25:38:47.7	J1229+0203	J1333+2725	1.482 ± 0.054	150.63
PG 1351+236	0.055	13:54:06.43	+23:25:49.1	J1229+0203	J1357+1919	0.974 ± 0.055	121.01
PG 1404+226	0.098	14:06:21.89	+22:23:46.6	J1229+0203	J1357+1919	0.900 ± 0.002	151.37
PG 1426+015	0.086	14:29:06.59	+01:17:06.5	J1337-1257/J1256-0547	J1408-0752/J1410+0203	2.158 ± 0.010	151.22
PG 1448+273	0.065	14:51:08.76	+27:09:26.9	J1337-1257/J1229+0203	J1446+1721/J1427+2348	0.642 ± 0.025	279.44
PG 1501+106	0.036	15:04:01.20	+10:26:16.2	J1517-2422/J1229+0203	J1504+1029	2.153 ± 0.051	150.69
PG 2130+099	0.061	21:32:27.81	+10:08:19.5	J2253+1608	J2147+0929	1.498 ± 0.075	124.17
PG 2209+184	0.070	22:11:53.89	+18:41:49.9	J2253+1608	J2232+1143	1.541 ± 0.162	152.28
PG 2214+139	0.067	22:17:12.26	+14:14:20.9	J2253+1608	J2232+1143	1.471 ± 0.071	150.71
PG 2304+042	0.042	23:07:02.91	+04:32:57.2	J2253+1608	J2327+0940/J2320+0513	0.435 ± 0.011	151.23

NOTE— (1) Source name. (2) Redshift. (3) Right ascension. (4) Declination. (5) Bandpass and flux calibrators; since each source is observed multiple times, more than one calibrator may be used for one source. (6) Phase calibrators. (7) The median and standard deviation of the precipitable water vapour (PWV). (8) Total on-source integration time.

Table 2. Summary of Observational Results

Object	$\log \lambda L_{\lambda}(5100 \text{ \AA})$ (erg s^{-1})	$\log M_{\text{BH}}$ (M_{\odot})	$\log M_{*}$ (M_{\odot})	q	Ref.	$S_{\text{CO}\Delta\nu}$ (Jy km s^{-1})	$\Delta S_{\text{CO}\Delta\nu}$ (σ_{total})	$\log L'_{\text{CO}(1-0)}$ ($\text{K km s}^{-1} \text{ pc}^2$)	$\log M_{\text{H}_2}$ (M_{\odot})	W_{50} (km s^{-1})	W_{20} (km s^{-1})	Prof.	$\log L_{\text{IR}}$ (erg s^{-1})	$\log M_{\text{gas}}$ (M_{\odot})
(1)	(2)	(3)	(4)	(5)	(6)	(7)	(8)	(9)	(10)	(11)	(12)	(13)	(14)	(15)
PG 0003+199	44.17	7.52	>10.00	0.93	1	1.49 ± 0.19	-0.058	7.26 ± 0.06	7.75 ± 0.30	$155.06^{+16.37}_{-14.67}$	$237.51^{+22.54}_{-21.95}$	S	$43.11^{+0.03}_{-0.03}$	8.32 ± 0.20
PG 0007+106	44.79	8.87	10.84	2.85 ± 0.31	-1.052	8.66 ± 0.05	9.15 ± 0.30	$386.78^{+29.57}_{-25.18}$	$460.52^{+47.60}_{-42.04}$	D	$44.27^{+0.02}_{-0.02}$	9.76 ± 0.22
PG 0049+171	43.97	8.45	>10.80	<0.88	...	<7.86	<8.35	$42.91^{+0.05}_{-0.05}$	8.66 ± 0.36
PG 0050+124	44.76	7.57	11.12	0.53	2	75.99 ± 0.80	-0.827	9.75 ± 0.01	10.24 ± 0.30	$377.77^{+0.85}_{-0.86}$	$431.59^{+1.47}_{-1.32}$	D	$44.94^{+0.01}_{-0.01}$	10.30 ± 0.20
PG 0093+129	43.83	7.52	10.71	0.78	2	32.24 ± 0.87	2.113	8.73 ± 0.01	9.22 ± 0.30	$361.68^{+1.07}_{-1.03}$	$387.27^{+1.87}_{-1.71}$	D	$44.05^{+0.01}_{-0.02}$	9.48 ± 0.20
PG 0934+013	43.85	7.15	10.38	0.69	2	6.72 ± 0.39	0.218	8.52 ± 0.03	9.02 ± 0.30	$217.84^{+7.98}_{-7.15}$	$290.73^{+10.24}_{-9.08}$	D	$43.96^{+0.02}_{-0.02}$	9.48 ± 0.20
PG 1011-040	44.23	7.43	10.87	0.92	2	16.20 ± 0.44	-0.205	9.04 ± 0.01	9.53 ± 0.30	$141.00^{+1.35}_{-1.12}$	$214.90^{+2.04}_{-2.08}$	S	$43.98^{+0.02}_{-0.02}$	9.65 ± 0.20
PG 1119+120	44.10	7.58	10.67	0.63	2	7.67 ± 0.28	-1.050	8.56 ± 0.02	9.06 ± 0.30	$212.68^{+2.41}_{-2.37}$	$236.69^{+3.78}_{-3.87}$	D	$44.12^{+0.02}_{-0.04}$	9.26 ± 0.20
PG 1126-041	44.36	7.87	10.85	16.04 ± 0.64	-0.592	9.06 ± 0.02	9.55 ± 0.30	$467.00^{+1.74}_{-1.72}$	$494.33^{+3.21}_{-3.25}$	D	$44.46^{+0.03}_{-0.03}$	9.65 ± 0.20
PG 1211+143	45.04	8.10	10.38	0.84	1	0.64 ± 0.05	-0.666	7.97 ± 0.03	8.46 ± 0.30	$65.90^{+7.00}_{-7.05}$	$100.94^{+11.40}_{-11.40}$	S	$43.32^{+0.05}_{-0.05}$	9.51 ± 0.29
PG 1229+204	44.35	8.26	10.94	0.55	1	4.73 ± 0.32	0.894	8.59 ± 0.03	9.08 ± 0.30	$202.21^{+3.14}_{-2.84}$	$223.50^{+5.55}_{-4.53}$	D	$43.96^{+0.01}_{-0.01}$	9.72 ± 0.20
PG 1244+026	43.77	6.62	10.19	0.70	2	6.14 ± 0.26	-2.003	8.45 ± 0.02	8.94 ± 0.30	$108.94^{+2.94}_{-2.91}$	$166.18^{+4.33}_{-4.75}$	S	$43.85^{+0.02}_{-0.01}$	8.78 ± 0.20
PG 1310-108	43.70	7.99	>10.40	3.87 ± 0.15	0.064	7.97 ± 0.02	8.46 ± 0.30	$204.08^{+7.04}_{-6.53}$	$258.09^{+10.67}_{-9.77}$	D	$43.16^{+0.02}_{-0.04}$	8.95 ± 0.20
PG 1341+258	44.31	8.15	>10.54	0.67 ± 0.15	0.173	8.01 ± 0.10	8.51 ± 0.31	$43.81^{+0.04}_{-0.05}$	9.32 ± 0.25
PG 1351+236	44.02	8.67	>10.98	19.17 ± 0.67	-2.093	9.06 ± 0.02	9.55 ± 0.30	$340.88^{+1.84}_{-1.81}$	$366.46^{+2.77}_{-3.03}$	D	$44.28^{+0.01}_{-0.01}$	9.77 ± 0.20
PG 1404+226	44.35	7.01	>9.56	4.80 ± 0.26	-0.584	8.97 ± 0.02	9.46 ± 0.30	$284.69^{+9.27}_{-8.60}$	$312.29^{+12.40}_{-11.86}$	D	$43.97^{+0.02}_{-0.02}$	9.99 ± 0.20
PG 1426+015	44.85	9.15	11.05	...	1	11.31 ± 0.56	-1.343	9.23 ± 0.02	9.72 ± 0.30	$343.71^{+10.16}_{-10.26}$	$524.34^{+14.76}_{-17.54}$	S	$44.55^{+0.02}_{-0.02}$	10.00 ± 0.20
PG 1448+273	44.45	7.09	10.47	0.63	2	4.45 ± 0.21	-0.374	8.58 ± 0.02	9.07 ± 0.30	$170.78^{+4.07}_{-4.27}$	$260.13^{+6.28}_{-6.91}$	S	$43.95^{+0.02}_{-0.02}$	9.17 ± 0.20
PG 1501+106	44.26	8.64	>10.96	1.30 ± 0.12	-1.416	7.52 ± 0.04	8.02 ± 0.30	$192.68^{+10.41}_{-9.49}$	$234.10^{+16.94}_{-14.06}$	D	$43.74^{+0.07}_{-0.05}$	8.69 ± 0.20
PG 2130+099	44.54	8.04	10.85	0.44	1	14.07 ± 0.39	-1.050	9.02 ± 0.01	9.51 ± 0.30	$548.36^{+4.68}_{-4.53}$	$600.61^{+8.20}_{-8.20}$	D	$44.37^{+0.03}_{-0.03}$	9.69 ± 0.20
PG 2209+184	44.44	8.89	>11.17	6.05 ± 0.26	0.613	8.77 ± 0.02	9.27 ± 0.30	$277.48^{+1.36}_{-1.22}$	$284.60^{+2.32}_{-2.32}$	D	$43.81^{+0.02}_{-0.03}$	10.07 ± 0.20
PG 2214+139	44.63	8.68	10.98	0.97	2	1.24 ± 0.13	2.489	8.05 ± 0.05	8.54 ± 0.30	$179.64^{+9.00}_{-8.89}$	$200.38^{+17.19}_{-11.13}$	D	$43.57^{+0.01}_{-0.02}$	9.56 ± 0.21
PG 2304+042	44.04	8.68	>10.99	<0.80	...	<7.45	<7.94	$42.66^{+0.06}_{-0.08}$	8.37 ± 0.27

NOTE— (1) Source name. (2) AGN monochromatic luminosity of the continuum at 5100 Å. (3) BH mass. (4) Stellar mass of the host galaxy. The uncertainty of the direct measurements is ~ 0.3 dex. The lower limits come from bulge masses estimated from the BH mass using the $M_{\text{BH}} - M_{\text{bulge}}$ relation. See Table 1 of Shanguan et al. (2018) for more details. (5) Axial ratio, derived from GALFIT modeling of the quasar host galaxies. (6) References for the axial ratio. (7) Integrated line flux of CO(2–1) emission. (8) The significance of the measured CO(2–1) fluxes deviate from those measured from the 15'' UV-tapered images. Positive deviation means the tapered flux larger than the flux in previous column. σ_{total} is the quadrature sum of the flux uncertainties. (9) CO line luminosity, converted from $J = (2-1)$ to $J = (1-0)$ with a line ratio of 0.62. (10) Molecular gas mass derived from CO line luminosity, assuming $\alpha_{\text{CO}} = 3.1 M_{\odot} (\text{K km s}^{-1} \text{ pc}^2)^{-1}$. (11) The width of the CO integrated profile at 50 percent of its maximum. (12) The width of the CO integrated profile at 20 percent of its maximum. (13) CO line profile: “S” = single-peaked profile and “D” = double-peaked profile. (14) IR luminosity of the host galaxy from spectral energy distribution decomposition by Shanguan et al. (2018). (15) Total gas mass derived from the dust mass. Columns (2)–(5) and (14) are collected from Table 1 of Shanguan et al. (2018). References: (1) Kim et al. (2017); (2) Y. Zhao et al. (in preparation).

Table 3. CO(2–1)/CO(1–0) Line Ratio

Object	$\log L'_{\text{CO}(1-0)}$ (K km s ^{−1} pc ²)	$\log L'_{\text{CO}(2-1)}$ (K km s ^{−1} pc ²)	R_{21}	$\langle U \rangle$	Ref.
(1)	(2)	(3)	(4)	(5)	(6)
PG 0003+199	<8.87	7.05±0.05	>0.02	15.16	1 ^a
PG 0007+106	<9.07	8.45±0.05	>0.24	7.95	2
PG 0050+124	9.74±0.02	9.54±0.01	0.63±0.02	10.07	3 ^b
PG 0934+013	<8.34	8.31±0.03	>0.93	7.20	4
PG 1011−040	9.05±0.04	8.83±0.01	0.60±0.05	5.10	4
PG 1119+120	8.50±0.06	8.35±0.02	0.71±0.11	17.57	3
PG 1126−041	9.12±0.04	8.85±0.02	0.53±0.05	15.36	4
PG 1211+143	<8.73	7.76±0.03	>0.11	2.00	5
PG 1229+204	8.69±0.11	8.38±0.03	0.49±0.13	4.02	5
PG 1310−108	<8.16	7.76±0.02	>0.40	3.98	4
PG 1404+226	8.98±0.11	8.76±0.02	0.60±0.15	2.39	5
PG 1426+015	9.12±0.07	9.02±0.02	0.79±0.14	8.32	5
PG 1501+106	<9.24	7.31±0.04	>0.01	25.48	1
PG 2130+099	8.85±0.06	8.81±0.01	0.90±0.12	11.04	3
PG 2214+139	<8.55	7.84±0.05	>0.19	2.55	5 ^a

^a $L'_{\text{CO}(1-0)}$ is considered an upper limit; archival measurement has poor S/N.

^b The line flux and FWHM of PG 0050+124 from [Evans et al. \(2006\)](#) are entirely consistent with those reported recently by [Tan et al. \(2019\)](#).

NOTE— (1) Object name. (2) The CO(1–0) line luminosity from the literature. (3) The CO(2–1) line luminosity from our ALMA observations (see Table 2). (4) The CO line luminosity ratio, $R_{21} \equiv L'_{\text{CO}(2-1)}/L'_{\text{CO}(1-0)}$. (5) The mean interstellar radiation field intensity derived from the IR spectral energy distribution of the quasar ([Shangguan et al. 2018](#)). (6) References: (1) [Maiolino et al. \(1997\)](#); (2) [Evans et al. \(2001\)](#); (3) [Evans et al. \(2006\)](#); (4) [Bertram et al. \(2007\)](#); (5) [Scoville et al. \(2003\)](#).

Table 4. Literature Sample

Object	z	$\log \lambda L_{\lambda}(5100 \text{ \AA})$ (erg s^{-1})	$\log M_{\text{BH}}$ (M_{\odot})	$\log M_{*}$ (M_{\odot})	q	Ref.	$S_{\text{CO}}\Delta\nu$ (Jy km s^{-1})	$\log L'_{\text{CO}}$ ($\text{K km s}^{-1} \text{ pc}^2$)	$\log M_{\text{H}_2}$ (M_{\odot})	W_{50} (km s^{-1})	W_{20} (km s^{-1})	Ref.	$\log L_{\text{IR}}$ (erg s^{-1})	$\log M_{\text{gas}}$ (M_{\odot})
(1)	(2)	(3)	(4)	(5)	(6)	(7)	(8)	(9)	(10)	(11)	(12)	(13)	(14)	(15)
PG 0052+251	0.155	45.00	8.99	11.05	0.55	2	2.0	9.39	9.88	429	500 ^a	3	$44.51^{+0.02}_{-0.02}$	10.29 ± 0.20
PG 0157+001	0.164	44.95	8.31	11.53	0.60	1	5.5 ± 0.5	9.88 ± 0.04	10.37 ± 0.30	270 ^a	315	4	$45.85^{+0.03}_{-0.05}$	10.80 ± 0.20
PG 0804+761	0.100	45.03	8.55	10.64	0.65	2	2.0 ± 0.5	9.00 ± 0.11	9.49 ± 0.32	755	881 ^a	5	$43.83^{+0.07}_{-0.05}$	8.79 ± 0.21
PG 0838+770	0.131	44.70	8.29	11.14	2.5 ± 0.4	9.34 ± 0.07	9.83 ± 0.31	60 ^a	70	4	$44.72^{+0.03}_{-0.04}$	10.21 ± 0.20
PG 0844+349	0.064	44.46	8.03	10.69	0.39	1	<1.5	<8.48	<8.97	5	$43.61^{+0.02}_{-0.02}$	10.01 ± 0.21
PG 1202+281	0.165	44.57	8.74	10.86	0.92	2	<2.4	<9.53	<10.02	6	$44.53^{+0.03}_{-0.03}$	9.51 ± 0.20
PG 1226+023	0.158	45.99	9.18	11.51	0.65	2	1.82 ± 0.02	9.37 ± 0.01	9.86 ± 0.30	490	572	8	$42.58^{+0.47}_{-0.57}$	9.11 ± 0.57
PG 1309+355	0.184	44.98	8.48	11.22	...	1	<0.6	<9.02	<9.51	3	$44.41^{+0.04}_{-0.04}$	10.40 ± 0.23
PG 1351+640	0.087	44.81	8.97	10.63	0.98	2	2.7 ± 0.5	9.01 ± 0.08	9.50 ± 0.31	260 ^a	303	4	$44.78^{+0.04}_{-0.05}$	9.67 ± 0.20
PG 1402+261	0.164	44.95	8.08	10.86	0.45	1	2.0	9.44	9.93	3	$45.01^{+0.04}_{-0.04}$	9.93 ± 0.20
PG 1411+442	0.089	44.60	8.20	10.84	0.71	1	<1.8	<8.85	<9.34	5	$44.14^{+0.03}_{-0.03}$	9.90 ± 0.21
PG 1415+451	0.114	44.53	8.14	>10.53	2.1 ± 0.3	9.14 ± 0.06	9.63 ± 0.31	90 ^a	105	4	$44.40^{+0.02}_{-0.01}$	9.73 ± 0.20
PG 1440+356	0.077	44.52	7.60	11.05	0.66	1	6.6 ± 0.6	9.29 ± 0.04	9.78 ± 0.30	310 ^a	362	4	$44.77^{+0.02}_{-0.01}$	9.95 ± 0.20
PG 1444+407	0.267	45.17	8.44	11.15	0.78	1	0.7	9.42	9.91	257	300 ^a	3	$44.97^{+0.05}_{-0.05}$	9.51 ± 0.24
PG 1545+210	0.266	45.40	9.47	11.15	...	1	<1.0	<9.57	<10.07	3	<44.03	<10.38
PG 1613+658	0.129	44.81	9.32	11.46	...	1	8.0 ± 0.6	9.83 ± 0.03	10.32 ± 0.30	400 ^a	467	4	$45.39^{+0.02}_{-0.02}$	10.56 ± 0.20
PG 1700+518	0.282	45.69	8.61	11.39	0.49	1	3.9 ± 0.7	10.22 ± 0.08	10.71 ± 0.31	260 ^a	303	7	$45.81^{+0.02}_{-0.05}$	10.64 ± 0.20

^a The line width was originally provided in the literature.

NOTE— (1) Source name. (2) Redshift. (3) AGN monochromatic luminosity of the continuum at 5100 Å. (4) BH mass. (5) Stellar mass of the host galaxy. The uncertainty of the direct measurements is ~ 0.3 dex. The lower limits come from bulge masses estimated from the BH mass using the $M_{\text{BH}} - M_{\text{bulge}}$ relation. See Table 1 of Shangguan et al. 2018 for more details. (6) Axial ratio, derived from GALFIT modeling of the quasar host galaxies. (7) References of the axial ratio. (8) Integrated line flux of CO(1–0) emission. (9) CO(1–0) line luminosity. (10) Molecular gas mass derived from CO line luminosity, assuming $\alpha_{\text{CO}} = 3.1 M_{\odot} (\text{K km s}^{-1} \text{ pc}^2)^{-1}$. (11) The width of the CO integrated profile at 50 percent of its maximum. (12) The width of the CO integrated profile at 20 percent of its maximum. The flagged line widths were originally provided in the literature; other values converted assuming $W_{20}/W_{50} = 1.17$. (13) References for the CO(1–0) measurements. (14) IR luminosity of the host galaxy from spectral energy distribution decomposition by Shangguan et al. (2018). (15) Total gas mass derived from the dust mass. Columns (2)–(5) and (15) are collected from Table 1 of Shangguan et al. (2018). References: (1) Kim et al. (2017); (2) Y. Zhao et al. (in preparation); (3) Casoli & Loinard (2001); (4) Evans et al. (2006); (5) Scoville et al. (2003); (6) Evans et al. (2001); (7) Evans et al. (2009); (8) Husemann et al. (2019).